

## LABORATORY TESTING AND MODELLING OF MAGNETORHEOLOGICAL ELASTOMERS IN TENSION MODE

Denys GUTENKO<sup>\*</sup>, Paweł ORKISZ<sup>\*\*</sup>, Bogdan SAPIŃSKI<sup>\*\*</sup>

<sup>\*</sup> Faculty of Electrical and Computer Engineering, Department of Automatics and Computer Science,  
Cracow University of Technology, Warszawska 24, 31-155, Krakow, Poland

<sup>\*\*</sup> Faculty of Mechanical Engineering and Robotics, Department of Process Control,  
AGH University of Krakow, Mickiewicza 30 av., 30-059 Krakow, Poland

[denys.gutenko@doktorant.pk.edu.pl](mailto:denys.gutenko@doktorant.pk.edu.pl), [orkisz@agh.edu.pl](mailto:orkisz@agh.edu.pl), [deep@agh.edu.pl](mailto:deep@agh.edu.pl)

*received 19 June 2023, revised 14 Septemeber 2023, accepted 18 October 2023*

**Abstract:** The study deals with experimental testing and estimating the modified Dahl model parameters of magnetorheological elastomers (MREs) differing in volumetric concentrations of carbonyl iron particles (CIP). The authors present briefly an overview of scientific reports relating to MREs research. Next, they describe the structure and magnetic properties of two fabricated MREs, which were investigated using a scanning electron microscope, a magnetometer and a gaussmeter. Then, they reveal the structure of a specially engineered test rig for materials sample examination and present a scenario of experiments. Next, the test results of the material's mechanical properties conducted in the absence and presence of a magnetic field were discussed. Then, they describe a modified Dahl model of the material followed by parameters estimation and validation procedure. Finally, the authors summarise the test results and outline further research steps.

**Key words:** magnetorheological elastomer, modified Dahl model, magnetic field, force, displacement, stiffness, estimation, parameter

### 1. INTRODUCTION

Among the so-called smart materials, one special place is occupied by magnetorheological materials such as fluids, elastomers and foams. Magnetorheological elastomers (MREs) possess field-dependent characteristics that allow them to be used in various application areas, including vibration isolators [1,2], soft robots [3], sensors [4], and so on. That is why, in recent years, research interests in MREs have grown rapidly. The studies have been focused on the material structure of the MREs, their field-dependent characteristics, operating modes and applications. By principle, the MREs are composed of magnetic particles in a non-magnetic elastic matrix. In addition to that, MRE formulations feature additives to affect their properties. For example, the addition of graphene oxide decreases their compressive modulus [5], and silane coupling agents lead to a more uniform distribution of magnetic particles in the matrix [6]. Another problem refers to the influence of particles' parameters, such as the shape [7,8], volume fraction [9] and particle size [10]. Moreover, MREs exhibit either isotropic or anisotropic structures depending on the manufacturing method. With the isotropic MREs, magnetic particles are arranged randomly. For comparison, the anisotropic MRE samples are seasoned in the presence of a magnetic field which leads to the formation of chains of magnetic particles aligned in the direction of the field. After the material hardens, the position of the particles is fixed, which causes these chains to remain in place. As such, anisotropic MREs exhibit different behaviours depending on the direction of the acting forces. Therefore, the influence of anisotropy remains a challenge [11]. The studies of MRE properties refer mainly to the influence of the magnetic field level on various mate-

rial parameters, for example, permeability [12,13], stick-slip effect [14] and durability [15].

MREs can be operated in at least one of the following modes: shear, squeeze (stretch) and active field. The mentioned modes are described in detail in Li et al. [16]. A number of studies involve the shear mode [17–22]; however, less attention has been paid to the field active mode [23] and the squeeze mode [24]. An important part of the research studies is modelling the MREs behaviour when exposed to magnetic fields. Such studies have been carried out using microscale models [7,22,25,26], phenomenological models [27] or hybrid models [20]. Most research workers use the following models: Kelvin–Voigt [24], Bouc–Wen [18,19,28], Dahl [27], LuGre [2], the four-parameter model [29] and their modifications.

The present study addresses the experimental tests of MREs and a new estimation procedure of the modified Dahl model parameters of the materials. The proposed procedure can be useful in the simulation of mechatronic systems considering MREs. To achieve that, two MREs with different volumetric concentrations of carbonyl iron particles (CIP) were fabricated, an original test rig was assembled and an assumed scenario of experiments was implemented.

The paper is structured as follows. In Section 2 the authors reveal the structure of the MRE samples and characterise their magnetic properties. Section 3 highlights the preparation of the MRE samples, describes the test rig experiment and discusses the materials' test results. Section 4 describes the modified Dahl model for representing the behaviour of MREs in the presence of magnetic fields and reveals the model parameter estimation procedure. Finally, conclusions are provided in Section 5.

## 2. STRUCTURE AND MAGNETIC PROPERTIES OF MATERIALS

To fabricate the two MRE samples, two basic components, CIP and Ecoflex 00-10 silicone rubber (platinum-catalysed silicon), were mixed thoroughly. Next, an attempt was made to remove the air bubbles using an ultrasonic homogeniser mixer. The degassed material was cured without a magnetic field at ambient temperature. The concentration of CIP by volume in the materials is appr. 26% (sample S1) and 30% (sample S2), respectively, similar to that suggested in Bastola and Hossain [17]. Both fabricated materials are isotropic.

The samples S1 and S2 were examined under the Versa 3D scanning electron microscope [30]. Particle morphology observations were recorded using a secondary electron detector. Since the samples are non-conductive materials, the measurements were made in the low vacuum mode, and steam was used as the gas. The operating parameters of the microscope were as follows: level of voltage for accelerating the electron beam at 17 kV, electron beam diameter (spot size) at 4.5 nm and water vapour pressure of 90 Pa. The microscope images showing the structures of the samples S1 and S2 are revealed in Fig. 1. It can be seen that in both cases, the magnetic particles are evenly distributed inside the elastic matrix, sometimes grouped into small clusters. Note that the structure of the samples contains a small air bubble not removed by the degassing procedure; see the detail marked in Fig. 1.

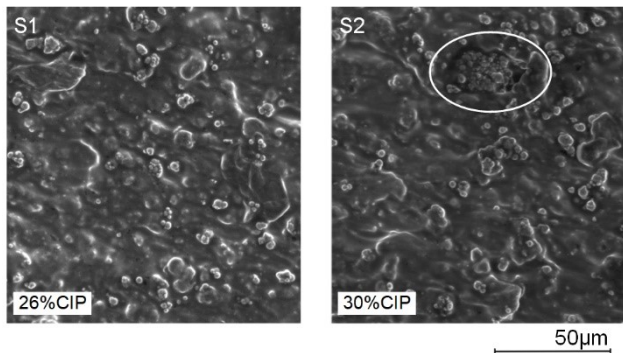


Fig. 1. Microscope images of samples: S1 and S2

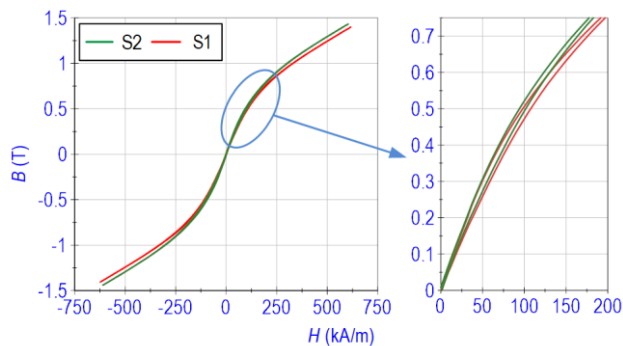


Fig. 2. Magnetic flux density B vs magnetic field strength H

Next, the magnetic tests of the samples, S1 and S2 (3 mm × 3 mm), were carried out using a LakeShore 7400 series vibrating sample magnetometer (VSM) [31] at two temperature levels: 0°C and 25°C. The temperature has no effect on the magnetisation

curves (within the examined range). Fig. 2 shows the obtained magnetisation curves B(H) for both samples. The hysteresis width is equal for both samples but the curves differ slightly (see the zoomed-in section in Fig. 2).

## 3. TESTING OF MATERIALS

The purpose of the material tests was to determine the relationship between their mechanical properties and the external stimuli affecting them. The tests of the MRE samples were carried out according to the diagram in Fig. 3a. Similar to the material in Section 2, we use the designations S1 and S2 to distinguish the MREs with differing concentrations of CIP by volume. The samples S1/S2 were placed between the movable platform and the force sensor (FS) to measure the displacement  $z$  and the resulting force  $F_m$ . Fig. 3b presents the sketch of the tested sample (4) with purpose-designed handles. It can be seen that the opposing surfaces of the sample were fixed to the handles using the cyanoacrylate glue layer (3). The handle consists of the plastic base (2), the nut (5) and the retaining screw (1). Fig. 3b also shows the dimensions of the fabricated sample and those of the handles.

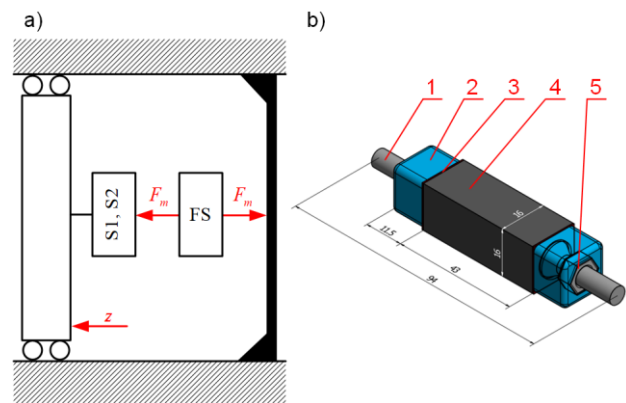


Fig. 3. MRE testing concept: (a) schematic diagram of the test rig concept, (b) MRE sample with handles

### 3.1. Preparation of samples

The samples were tested in the absence and presence of a magnetic field induced by NdFeB N38 neodymium magnets. Due to the installation of the permanent magnets, the plastic housing was designed and 3D printed. The housing was attached to the upper plastic base (see component 2 in Fig. 3b) using four screws. Fig. 4a,b shows the magnet housing view and its dimensions, respectively. The size of the housing (1) allows for an air gap of 0.5 mm between the sample (3) and the housing. Additionally, the housing ensures that the two magnets (2) can be placed symmetrically on the sample's opposite surfaces. Both magnets were of cylindrical shape and axially magnetised. The dimensions of the magnets are provided in Fig. 4b.

The testing of the samples (S1 and S2) was preceded by determining the magnetic flux density distribution in their surrounding using the Finite Element Method Magnetics package (FEMM) [32]. The simulations were conducted in a cartesian coordinate system, taking into account the measured non-linear magnetisation curves shown in Fig. 2. The magnet housing (1) (see Fig. 4a) and the

plastic base (2) (see Fig. 3b) were made using non-magnetic PLA filament, and their magnetisation characteristics were those of air. The retaining screw (1) (see Fig. 3b) was modelled using the stainless steel 316 material characteristics, while the magnets (2) (see Fig. 4a) were modelled by means of the N30 material B-H curve, assuming a coercivity of 686.4 kA/m. The planar model depth was equal to 15 mm.

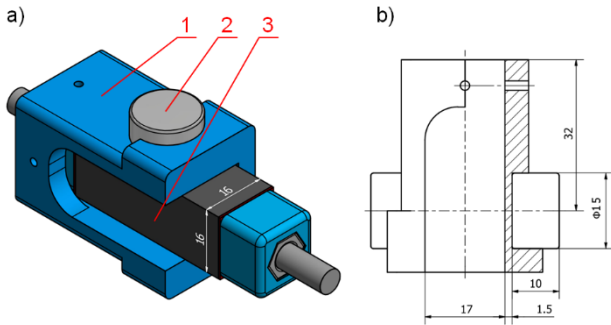


Fig. 4. Magnet housing: (a) view, (b) cross-section

Taking into account the designations  $B_x$  and  $B_y$  of the magnetic flux density components, the resultant magnetic flux density  $B$  can be expressed as:

$$B = \sqrt{B_x^2 + B_y^2} \quad (1)$$

The distribution of magnetic flux density  $B$  in the sample S1 is illustrated in Fig. 5. It can be seen that the lines of magnetic flux density were deformed to a small extent by the MRE sample.

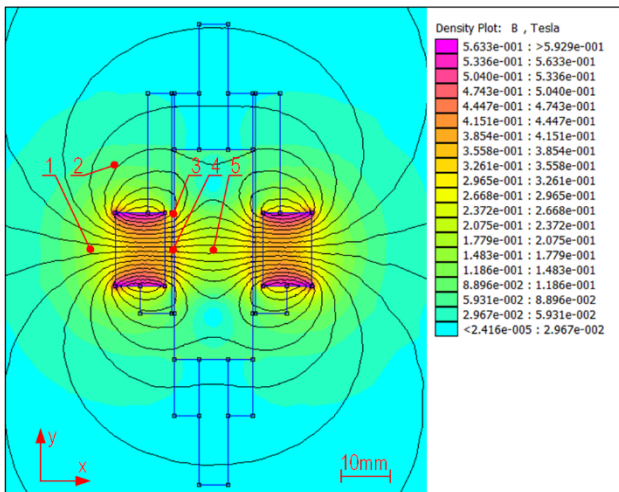


Fig. 5. Distribution of magnetic flux density  $B$ : sample S1

The values of  $B_x$  and  $B_y$  were interpreted at five points marked in Fig. 5 by the numbers 1, 2, 3, 4 and 5 and are provided in Tab. 1 for the samples S1 and S2 in columns 2 and 3. Accordingly, the numbers in column 4 were obtained by measuring the sample S1 using the gaussmeter GM2 [33] with a standard Hall probe.

Points 1 and 2 were selected only for verification purposes, whereas points 3 and 4 can be used for interpreting the values of magnetic flux density near the left magnet's housing wall. Point 5

is located in the sample's centre. The test results provided in Tab. 1 for the samples S1 and S2 are similar. Considering the values in the blue cells, the authors drew the following conclusions. Due to the limitations of the FEMM package and the cylindrical shape of the employed magnets, the best correlation between the simulation results and the test data was achieved at points 1,4 and 5. In the worst cases, the differences occurring at points 2 and 3 do not exceed 48 mT.

Tab. 1. Components  $B_x$  and  $B_y$  at the selected measurement points

Point no.	FEMM, S1 mT		FEMM, S2 mT		GM2, S1 mT	
	$B_x$	$B_y$	$B_x$	$B_y$	$B_x$	$B_y$
1	175	-2	176	-2	175	-
2	-53	-63	-54	-64	-	-32
3	136	125	138	120	185	-
4	361	0	366	0	370	-
5	219	0	220	0	183	-

"-" no space available for measurements

### 3.2. Test rig

For further examinations of the samples, a special test rig was assembled (see Fig. 6). In the rig, two main modules can be distinguished: the mechanical rig and the electrical module (actuation). The mechanical rig consists of an aluminium frame (10) and linear guides along which three movable platforms move. The vibration shaker platform (3) was used for generating the excitation (displacement)  $z$  using the electrodynamic linear LA30 motor (2) [34]. The middle platform (9) was fixed and was used only to eliminate the clearance directly upon the assembly of the tested sample. Platform (11) was not utilised in the test program.

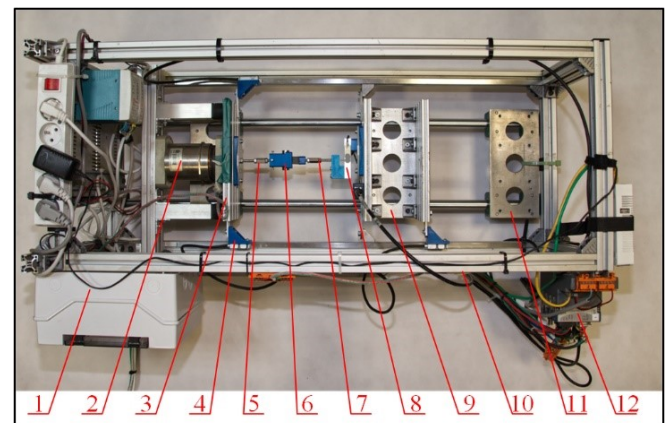


Fig. 6. View of the test rig

The electrical module of the rig was composed of the power supply unit (1), the cRIO 9063 controller (12) [35], the personal computer and the three dedicated measurement boards connected with the following components:

- NI-9505 motor drive module to generate the displacement  $z$ ;
- NI 9237 strain full bridge input module to measure the force  $F_m$  using the NA27 strain gauge beam (8) calibrated within the range of  $\pm 10N$  and attached to the fixed platform;

- NI-9215 analogue input module to measure the displacement  $z$  using the linear encoder (4) [36].

The architecture of the control software developed in the LabVIEW environment is described in Snamina and Orkisz [37]. The tested sample with the magnet handle (see Fig. 4a and component 6 in Fig. 6) was equipped with the fixtures (5) and (7), and mounted between the shaker platform and the strain gauge beam.

### 3.3. Scenario of tests

The tests were split into two stages. In the first stage, the authors measured the response of the samples subjected to static excitations. First, the samples were excited sinusoidally using an amplitude of  $A_z = 3$  mm and at a frequency of  $f = 0.1$  Hz. Next, the authors measured the response of the samples to dynamic excitations. The samples were excited sinusoidally at three different amplitude levels:  $A_z$  0.4 mm, 0.6 mm and 0.8 mm, and the frequency of the sinewave was slowly increased from 0.3 Hz to 10 Hz. The tests were carried out at a temperature of 25°C. The sampling frequency was  $f_p = 4$  kHz.

Due to the high sampling frequency, the test results were filtered using a moving average filter (the window width was 20 samples). The precision of the displacement measurements expressed with the standard deviation value of the displacement  $z$  was  $2.88 \cdot 10^{-4}$  mm and the standard deviation value of the measured force  $F_m$  was  $1.85 \cdot 10^{-3}$  N. The tests were implemented several times for each sample, taking into account the influence of the magnetic field and the input displacement amplitude  $A_z$ .

To simplify the interpretation of the test results, the authors introduced the following designation  $SX_{A_z}^{MY}$  where  $X$  refers to the sample number,  $A_z$  denotes the displacement amplitude and  $MY$  refers to the level of magnetic field;  $Y = 0$  – no magnetic field and  $Y = 1$  – magnetic field applied.

### 3.4. Results and discussion

The results of the static tests were obtained by recording the behaviour of the samples during five 10-second excitation cycles. Fig. 7 shows exemplary time patterns of the displacement  $z$  and the force  $F_m$  for the sample S1 in the cases M0 and M1. Next, the recorded results were used to determine the force–displacement loops  $F_m(z)$  shown for the sample S1 in Fig. 8 and for the sample S2 in Fig. 9.

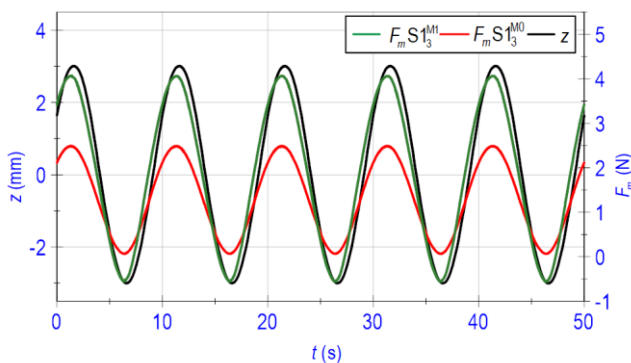


Fig. 7. Time histories of displacement  $z$  and force  $F_m$ : sample S1

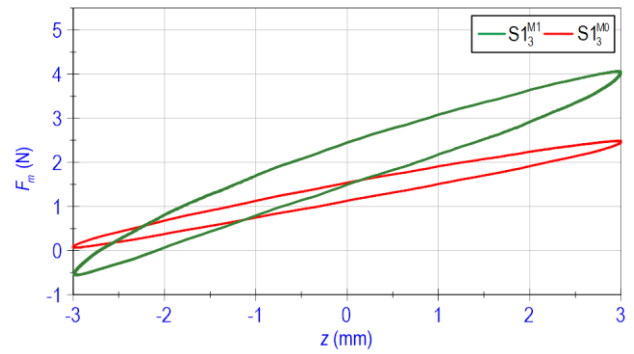


Fig. 8. Force  $F_m$  vs displacement  $z$ : sample S1

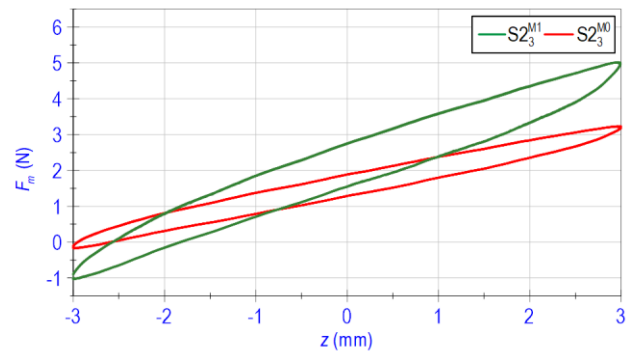


Fig. 9. Force  $F_m$  vs displacement  $z$ : sample S2

Taking into account the plots in Figs. 8 and 9, the length of the sample  $d = 43$  mm and the cross-sectional area of the sample  $a_s = 256$  mm<sup>2</sup>, the sample deformation  $\epsilon_s$  expressed in percents was calculated as follows:

$$\epsilon_s = \frac{z + \max(z)}{d} \cdot 100 \quad (2)$$

while the tensile stress  $\sigma_s$  was computed according to the following formula:

$$\sigma_s = \frac{F_m}{a_s} \quad (3)$$

The equivalent stiffness coefficient  $k_s$  was then calculated as:

$$k_s = \frac{A_{F_m}}{A_z} \quad (4)$$

where  $A_{F_m}$  is the force amplitude and  $A_z$  is the displacement amplitude. Similarly, the equivalent damping coefficient  $c_s$  was calculated as follows:

$$c_s = \frac{A_{F_m}}{A_z} \quad (5)$$

where  $A_z$  refers to the velocity amplitude. The value of the hysteresis coefficient  $h_s$  was calculated using the formula:

$$h_s = 0.5 \cdot [F_m(z_0^\uparrow) - F_m(z_0^\downarrow)] \quad (6)$$

where  $F_m(z_0^\uparrow)$  is the force registered for the increasing displacement  $z$  at the value of 0 mm and  $F_m(z_0^\downarrow)$  refers to force registered for the decreasing displacement  $z$  at the same value.

Tab. 2. Test results

Sample no.	Range of $\epsilon_s$ %	Range of $\sigma_s$ kPa	$k_s$ N/mm	$c_s$ N·s/mm	$h_s$ N
S1 <sub>3</sub> <sup>M0</sup>	0, 13.95	0.27, 9.70	0.40	0.64	0.205
S1 <sub>3</sub> <sup>M1</sup>	0, 13.95	-2.10, 15.87	0.77	1.23	0.475
S2 <sub>3</sub> <sup>M0</sup>	0, 13.95	-0.64, 12.65	0.57	0.91	0.300
S2 <sub>3</sub> <sup>M1</sup>	0, 13.95	-4.00, 19.58	1.01	1.61	0.600

The results obtained using the assumed excitations are provided in Tab. 2. In each case, the values of the sample deformations  $\epsilon$  vary within the range from 0% to 13.95%. The value of the tensile stress  $\sigma_s$  does not exceed 20 kPa. The equivalent stiffness coefficient  $k_s$ , the equivalent damping coefficient  $c_s$  and the hysteresis coefficient  $h_s$  depend on the magnetic flux density level and the CIP volume. The higher CIP content sample is characterised by a greater increase of the equivalent stiffness coefficient, the equivalent damping coefficient as well as the higher value of the hysteresis coefficient  $h_s$ .

The results also revealed the effect of long-term exposure of the samples to the magnetic field (residual magnetism). For the sample subjected to magnetic field for at least 6 h, regardless of the displacement  $z$ , a constant increase in the force  $F_m$  of 0.15 N was observed. The data provided in Tab. 2 relate to the behaviour of the samples subjected to constant amplitude and constant frequency excitations. Considering the non-linear nature of the MREs, dynamic tests were conducted under sinusoidal excitations of the amplitudes  $A_z$  of 0.4 mm, 0.6 mm and 0.8 mm. The plot of the equivalent stiffness coefficient  $k_s$  versus the frequency  $f$  was adopted, following formula (3) and taking into account that the ratio of  $A_{Fm}$  to  $A_z$  was dependent on the excitation frequency. Fig. 10 shows the test results for the sample S1 and Fig. 11 reveals the data obtained for the sample S2.

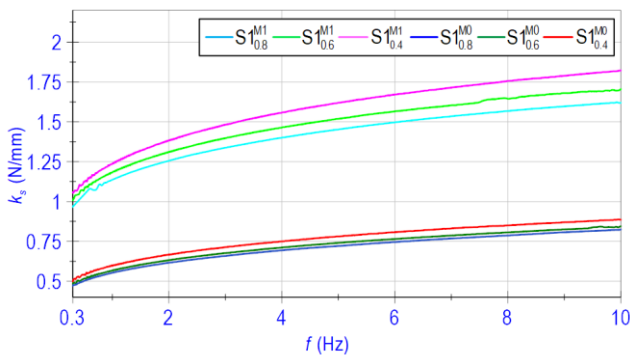


Fig. 10. Equivalent stiffness coefficient  $k_s$  versus frequency  $f$ : sample S1

The results reveal, on one hand, that an increase in the frequency  $f$  results in an increase in the equivalent stiffness coefficient  $k_s$ . On the other hand, the increase in amplitude  $A_z$  causes a decrease in the coefficient  $k_s$ . Next, Tab. 3 provides the impact of the concentrations of CIP by volume on the coefficient  $k_s$ , and Fig. 12 shows the comparison between the coefficient  $k_s$  values obtained for both samples. The parameter  $k_d^{M0}$  in Tab. 3 designates the differences between the values of  $k_s$  in the case of S2<sub>0.4</sub><sup>M0</sup> and S1<sub>0.4</sub><sup>M0</sup>, while the  $k_d^{M1}$  designates the differences between

the values of  $k_s$  in the case of S2<sub>0.4</sub><sup>M1</sup> and S1<sub>0.4</sub><sup>M1</sup>. It is apparent that the values of  $k_d^{M0}$  and  $k_d^{M1}$  were nearly equal at frequencies above 3 Hz. Therefore, the differences between the values of the stiffness coefficient  $k_s$  for the samples S1 and S2 depend mostly on the magnetic field level and to a slight extent on the volume of CIP particles.

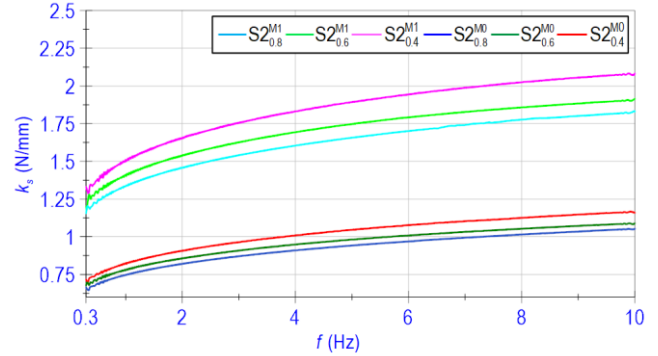


Fig. 11. Equivalent stiffness coefficient  $k_s$  versus frequency  $f$ : sample S2

Tab. 3. Equivalent stiffness coefficient versus frequency

Freq. $f$ Hz	$k_s$ S1 <sub>0.4</sub> <sup>M1</sup> N/mm	$k_s$ S2 <sub>0.4</sub> <sup>M0</sup> N/mm	$k_d^{M0}$ N/mm	$k_s$ S1 <sub>0.4</sub> <sup>M1</sup> N/mm	$k_s$ S2 <sub>0.4</sub> <sup>M1</sup> N/mm	$k_d^{M1}$ N/mm
1	0.60	0.83	0.23	1.24	1.50	0.26
3	0.71	0.96	0.25	1.48	1.76	0.28
5	0.78	1.05	0.27	1.62	1.89	0.27
7	0.83	1.11	0.28	1.71	1.99	0.28
9	0.87	1.15	0.28	1.79	2.06	0.27

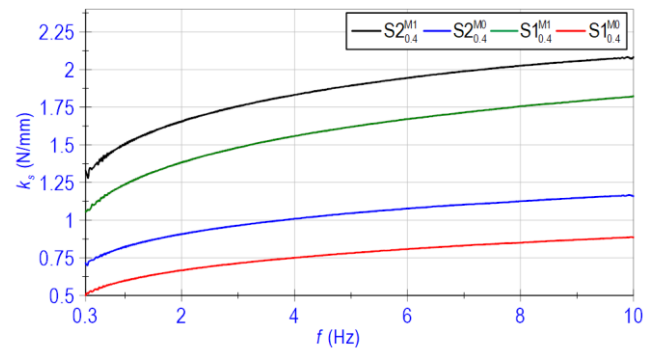


Fig. 12. Equivalent stiffness coefficient  $k_s$  versus frequency  $f$ : samples S1, S2

#### 4. MODIFIED DAHL MODEL OF MATERIALS

Most parametric models in field-dependent behaviour of MREs are based on Kelvin–Voigt, Bouc–Wen, Dahl, LuGre and four-parameter viscoelastic models. Among the models that concern the description of the hysteresis phenomenon, the Dahl model considers fewer parameters whose values must be estimated, making it computationally more efficient. In this work, the authors select for analysis the modified Dahl model with the structure shown in Fig. 13.

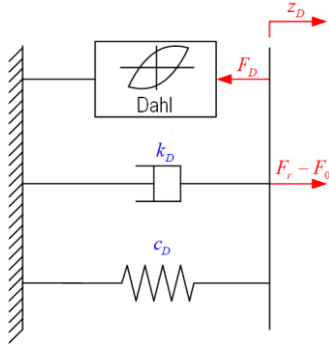


Fig. 13. Structure of the modified Dahl model

The model can be described as follows:

$$F_r = F_D + c_D \dot{z}_D + k_D z_D + F_0 \quad (7)$$

where  $z_D$  is the displacement,  $c_D$  denotes the damping coefficient and  $k_D$  refers to the stiffness coefficient. As it can be seen, the force  $F_r$  incorporates four components, namely the Dahl model friction force  $F_D$ , the viscous force  $c_D \dot{z}$ , the spring force  $k_D z$  and offset in the force  $F_0$ . The component  $F_D$  is expressed using the following formula:

$$\frac{\partial F_D}{\partial z_D} = \sigma \left[ 1 - \frac{F_D}{h_D} \operatorname{sgn} \left( \frac{dz_D}{dt} \right) \right]^b \quad (8)$$

where  $\sigma$  represents the Dahl's model stiffness coefficient,  $b$  describes the shape of the stress-strain curve and  $h_D$  is the Coulomb friction force. Assuming that  $\rho = \frac{\sigma}{h_D}$ ,  $r = F_D/h_D$  and  $b = 1$  [38], equation (8) can be rewritten as:

$$\dot{r} = \rho (\dot{z}_D - r |\dot{z}_D|) \quad (9)$$

Let us consider that displacement  $z_D$  varies sinusoidally with the amplitude  $A_{zD}$  and frequency  $f_{zD}$  in one cycle:

$$z_D(t) = -A_{zD} \cdot \cos(2\pi f_{zD} t) \quad (10)$$

Then, in the first half of the displacement cycle period, the value of  $z_D$  increases from  $-A_{zD}$  to  $A_{zD}$ , whereas in the second half of the period this value decreases. Following Eq. (10), the velocity takes the form:

$$v_D(t) = 2\pi f_{zD} A_{zD} \sin(2\pi f_{zD} t) \quad (11)$$

Combining Eqs (7, 9–11), the modified Dahl model can be written as:

$$\begin{cases} F_r(t) = h_D r + c_D v_D(t) + k_D z_D(t) + F_0 \\ \dot{r}(t) = \rho (v_D(t) - r |v_D(t)|) \end{cases} \quad (12)$$

It is evident then that the model contains seven parameters ( $k_D, c_D, h_D, \rho, A_{zD}, f_{zD}, F_0$ ). Three of them,  $A_{zD}, f_{zD}$  and  $F_0$ , may be determined directly from the test results, whereas the remaining parameters have to be estimated. Designating the sampling time by  $t_{pr}$ , the number of samples can be calculated according to:

$$n = \frac{1}{f_{zD} t_{pr}} \quad (13)$$

Using Eq. (12) in the simulations, the authors assumed the constant sampling time  $t_{pr}$ , and the initial condition  $r(0) = -1$ . The initial condition estimate was set to avoid initial errors and

improve the calculations' accuracy.

Considering the differences in the phase time pattern of the displacements  $z(t)$  and  $z_D(t)$ , the authors proposed to correct the time shift of the displacement  $z$  and force  $F_m$  by the value of  $\Delta t_m$ . Introducing displacement  $z_\Delta(t) = z(t - \Delta t_m)$  and force  $F_{m\Delta}(t) = F_m(t - \Delta t_m)$  the accuracy of the modified Dahl model can be evaluated by the following quality factor:

$$J_e = \sqrt{\frac{1}{n t_{pr}} \int_0^{n t_{pr}} (F_r(t) - F_{m\Delta}(t))^2 dt} \quad (14)$$

To achieve a better accuracy of the factor  $J_e$ , the scaling factor  $s_c = 0.5(|\sin(2\pi f_{zD} t)| + 1)$  was used and then, the modified quality factor could be expressed as follows:

$$J_{es} = \sqrt{\frac{\int_0^{n t_{pr}} (0.5(|\sin(2\pi f_{zD} t)| + 1) \cdot (F_r(t) - F_{m\Delta}(t))^2) dt}{n t_{pr}}} \quad (15)$$

Taking into account the shape of the relationship  $F_{m\Delta}(z_\Delta)$ , the benefit of the quality factor  $J_{es}$  is in reducing the weight factor for the samples located at the maximum and minimum values of the displacement  $z_\Delta$ , respectively. Such modification yields an improved projection of the model on the test results.

#### 4.1. Estimation procedure of model parameters

The proposed procedure for the estimation of the modified Dahl model parameters (see Fig. 14) consists of the following four stages:

- Stage 1. Data import and estimation of parameters  $A_{zD}, f_{zD}, F_0, \Delta t_m$ . The stage consists of two steps.
  - Step 1. Test results are imported considering the displacement  $z$  and the force  $F_m$ .
  - Step 2. The  $A_{zD}$  is determined as  $0.5 \cdot (\max(z) - \min(z))$ , the  $f_{zD}$  is calculated using the autocorrelation function,  $\Delta t_m$  is estimated using the cross-correlation function taking into consideration the displacements  $z(t)$  and  $z_D(t)$ ,  $F_0$  is computed by averaging  $F_m(t)$  over one cycle.
- Stage 2. Initial estimation of parameters  $k_D, c_D, h_D, \rho$ . The stage consists of three steps.
  - Step 1. Parameter initialisation. The one hundred sets of the parameters  $k_D, c_D, h_D, \rho$  were randomly selected within the corresponding ranges:  $k_D \in [0, 1.2]$  N/mm,  $c_D \in [0, 1.8]$  N-s/mm,  $h_D \in [0, 0.7]$  N,  $\rho \in [1, 2]$  s/mm. The ranges of  $k_D, c_D$  and  $h_D$  are selected based on Tab. 2, whereas the range of the parameter  $\rho$  is selected in order to preserve the shape of  $r(z_D)$ .
  - Step 2. Calculation of the force  $F_r(t)$  and the quality factor  $J_{es}$  using previously generated sets of parameters.
  - Step 3. Selection of the set of parameters for which the smallest value of the  $J_{es}$  factor was obtained. For further calculations, the selected set is referred to as  $S_b$ .
- Stage 3. Improvement of parameter estimation. The stage consists of four steps.
  - Step. 1 The parameter modification. Taking into account the set  $S_b$ , one to three of the parameters are randomly selected for modification. The modification considers random changes of the parameter value varying from 0 to twice its obtained value.
  - Step 2. Calculation of the force  $F_r(t)$  and the quality factor  $J_{es}$

- based on the formerly modified parameters.
- Step 3. Selection of the best-fitted set of parameters. If the value of  $J_{es}$  calculated for the set of modified parameters is less than the factor  $J_{es}$  calculated for the set  $S_b$ , then the modified set of parameters is considered as the new set  $S_b$ .
- Step 4. Steps 1–3 are repeated  $10^5$  times.
- Stage 4. Non-linear least-squares method application. The stage consists of two steps.
  - Step 1. The parameter set  $S_b$  is used as an initial condition in the lsqcurvefit function in MATLAB to calculate the modified set of parameters.
  - Step 2 If the value of the quality factor  $J_{es}$  determined for the set of parameters in Step 1 is smaller than the value obtained for the set  $S_b$ , then Stage 4 should be skipped.

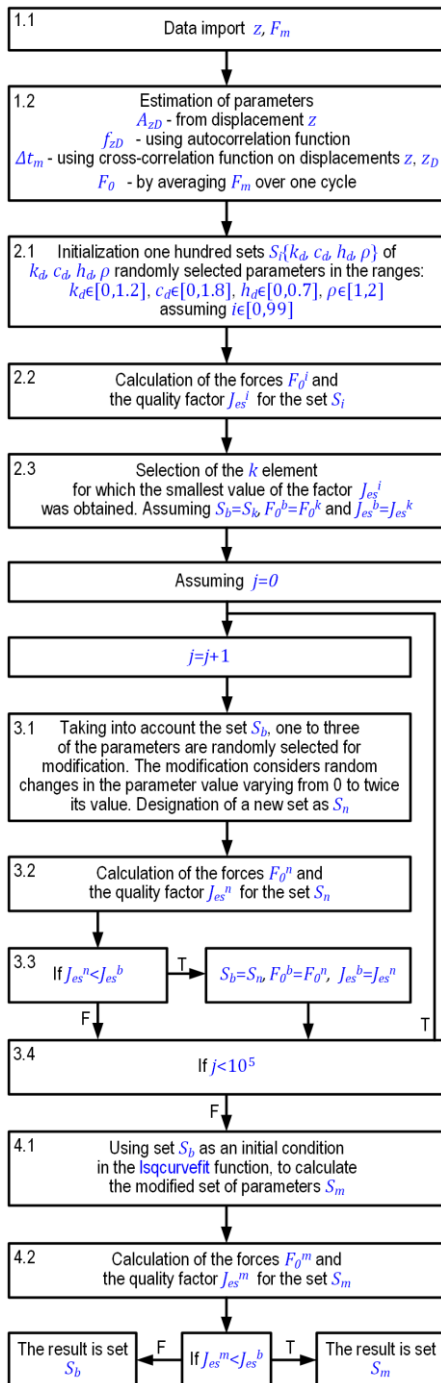


Fig. 14. Block diagram of the estimation procedure

## 4.2. Validation of procedure

The procedure elaborated in Subsection 4.1 was validated by comparing the simulation data obtained with the model against the test results.

The input to the procedure was the time patterns of the displacement  $z$  and force  $F_m$  registered for the sample  $S1_3$  (see Fig. 7). Two cases were considered, M0 and M1, which refer to both the absence and presence of the magnetic field. The procedure was repeated 10 times for both cases.

The validation results are shown in the form of force–displacement loops (see Figs. 15,16). In addition to that, in Tab. 4 the authors provide the calculated values (averaged over the set of realisations) to summarise each stage of the procedure.

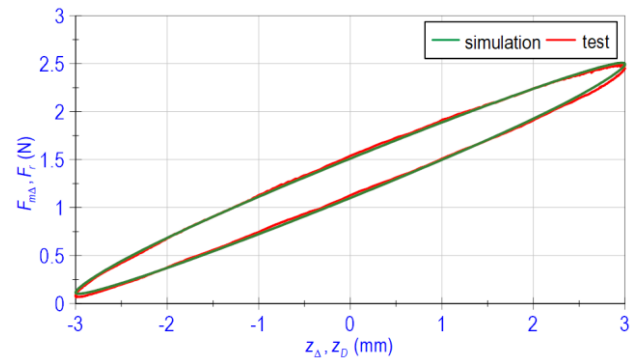


Fig. 15. Validation of the model:  $S1_3^{M0}$

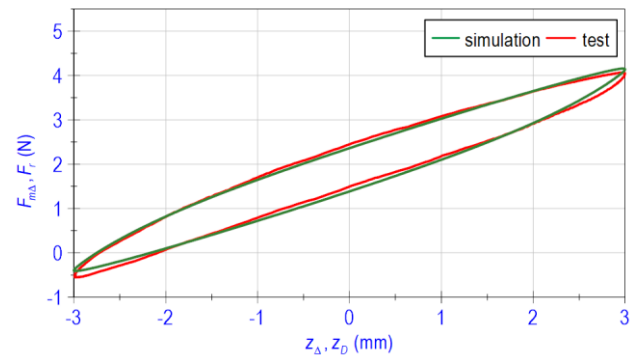


Fig. 16. Validation of the model:  $S1_3^{M1}$

Tab. 4. Parameter estimates: sample  $S1_3$

Stage no.	Model parameters	Quality factors
Case M0		
1	$A_{zD} = 3.01$ mm, $f_{zD} = 0.099$ Hz, $F_0 = 1.3$ N, $\Delta t_m = 6.63$ s.	-
2	$k_D = 0.3494$ N/mm, $c_D = 0.0811$ N·s/mm, $h_D = 0.1972$ N, $\rho = 1.59$ s/mm.	$J_e = 0.20002$ N, $J_{es} = 0.16608$ N.
3	$k_D = 0.3819$ N/mm, $c_D = 0.0886$ N·s/mm, $h_D = 0.0409$ N, $\rho = 1.46$ s/mm.	$J_e = 0.01673$ N, $J_{es} = 0.01351$ N.

4	$k_D = 0.3834$ N/mm, $c_D = 0.0912$ N-s/mm, $h_D = 0.0353$ N, $\rho =$ $1.46$ s/mm.	$J_e = 0.01666$ N, $J_{es} = 0.01345$ N.
Case M1		
1	$A_{zD} = 2.99$ mm, $f_{zD} = 0.1$ Hz, $F_0 = 1.85$ N, $\Delta t_m = 6.64$ s.	-
2	$k_D = 0.6602$ N/mm, $c_D = 0.1130$ N-s/mm, $h_D = 0.2906$ N, $\rho =$ $1.41$ s/mm.	$J_e = 0.14802$ N, $J_{es} = 0.11682$ N.
3	$k_D = 0.6784$ N/mm, $c_D = 0.1343$ N-s/mm, $h_D = 0.2372$ N, $\rho =$ $1.46$ s/mm.	$J_e = 0.06506$ N, $J_{es} = 0.05300$ N.
4	$k_D = 0.6797$ N/mm, $c_D = 0.1374$ N-s/mm, $h_D = 0.2309$ N, $\rho =$ $1.44$ s/mm.	$J_e = 0.06511$ N, $J_{es} = 0.05296$ N.

The comparison of the plots in Figs. 15,16 shows that a good agreement was achieved between the simulation data and the test results. Some insignificant inaccuracies could be observed only for the values of the force  $F_r$  which relate to the maximal and minimal values of the displacement  $z_D$ . The best-fitted parameter set of the model is marked in blue in Tab. 4. It is apparent that the values of the quality factors  $J_e$  and  $J_{es}$  took a less and less value at each stage, which confirms the accuracy of the estimation procedure. Moreover, the values of the parameters  $A_{zD}$  and  $f_{zD}$ , correspond to the values of  $A_z$  and  $f$  obtained from the tests. It can be seen that when comparing the case M1 against the case M0, the values of the stiffness coefficient  $k_D$  and the damping coefficient  $c_D$  increase by 0.3 N/mm and 0.046 N-s/mm. Furthermore, the parameter  $h_D$  assumes a small value, and, effectively, the developed models may resemble the Kelvin–Voigt model. The determined values of the parameter  $\rho$  vary mostly within the assumed range of [1,2] s/mm in the case of M0 and M1. Keeping in mind that  $\sigma = h_D \rho$ , a small value of the parameter  $h_D$  has an adverse effect on the estimation of the parameter  $\rho$ . The minimal and maximal values of parameters  $k_D$ ,  $c_D$ ,  $h_D$ ,  $\rho$  based on the set of realisations estimated at Stage 4 are provided in Tab. 5.

**Tab. 5.** Min/max values of the parameters obtained at Stage 4

Parameters	Case M0	Case M1
Min( $k_D$ )	0.3800 N/mm	0.6689 N/mm
Max( $k_D$ )	0.3856 N/mm	0.6899 N/mm
Min( $c_D$ )	0.0892 N-s/mm	0.1285 N-s/mm
Max( $c_D$ )	0.0937 N-s/mm	0.1492 N-s/mm
Min( $h_D$ )	0.0286 N	0.1993 N
Max( $h_D$ )	0.0442 N	0.2598 N
Min( $\rho$ )	0.99 s/mm	1.18 s/mm
Max( $\rho$ )	1.85 s/mm	1.68 /mm

## 5. CONCLUSION

This study deals with experimental tests and modelling of two fabricated MRE samples with different concentrations of CIP by volume. The work presents the microscopic examination of the material samples, discusses the influence of the magnetic field on the MRE samples' behaviour and proposes the estimation procedure of the modified Dahl model parameters.

The outcome of the research leads the authors to the following conclusions:

- The CIP inside the fabricated samples is regularly distributed in the silicon matrix, but the matrix contains inclusions of small air bubbles.
- The difference between the magnetisation curves of the examined samples results from different CIP contents.
- The equivalent stiffness and damping coefficients of the samples depend on the magnetic field level and the concentration of CIP by volume.
- The modified quality factor  $J_{es}$  increases the accuracy of the model parameters' determination in the zones close to the zero value of the displacement  $z_D$ .
- The estimated parameters of the modified Dahl model guarantee the reproduction of the real behaviour of the investigated sample.
- The multi-stage estimation procedure was proposed by the authors due to the potential application of more complex models such as Bouc–Wen or LuGre model.

The ongoing research will be focused on the extended test conditions to develop an inverse model of the manufactured MREs. The authors intend to investigate the influence of the magnetic flux density, amplitude and excitation frequency on the material behaviour.

## REFERENCES

1. Brancati R, Di Massa G, Pagano S, Santini S. A magneto-rheological elastomer vibration isolator for lightweight structures. *Meccanica* 2019;54:333–49. <https://doi.org/10.1007/s11012-019-00951-2>
2. Yu Y, Li Y, Li J. Parameter identification and sensitivity analysis of an improved LuGre friction model for magnetorheological elastomer base isolator. *Meccanica* 2015;50:2691–707. <https://doi.org/10.1007/s11012-015-0179-z>
3. [Gutenko D. State of the art of soft robotic applications based on magneto-rheological materials. *MATEC Web Conf* 2020;322:01050. <https://doi.org/10.1051/mateconf/202032201050>
4. Hu T, Xuan S, Ding L, Gong X. Stretchable and magneto-sensitive strain sensor based on silver nanowire-polyurethane sponge enhanced magnetorheological elastomer. *Mater Des* 2018;156:528–37. <https://doi.org/10.1016/j.matdes.2018.07.024>
5. Zhang G, Zhang J, Guo X, Zhang M, Liu M, Qiao Y, et al. Effects of graphene oxide on microstructure and mechanical properties of isotropic polydimethylsiloxane-based magnetorheological elastomers. *Rheol Acta* 2022;61:215–28. <https://doi.org/10.1007/s00397-022-01329-0>
6. Kashima S, Miyasaka F, Hirata K. Novel Soft Actuator Using Magnetorheological Elastomer. *IEEE Trans Magn* 2012;48:1649–52. <https://doi.org/10.1109/TMAG.2011.2173669>
7. Keip M-A, Rambauek M. Computational and analytical investigations of shape effects in the experimental characterization of magnetorheological elastomers. *Int J Solids Struct* 2017;121:1–20. <https://doi.org/10.1016/j.ijsolstr.2017.04.012>




8. Samal S, Blanco I. Investigation of Dispersion, Interfacial Adhesion of Isotropic and Anisotropic Filler in Polymer Composite. *Appl Sci* 2021;11:8561. <https://doi.org/10.3390/app11188561>
9. Vatandoost H, Rakheja S, Sedaghati R. Effects of iron particles' volume fraction on compression mode properties of magnetorheological elastomers. *J Magn Magn Mater* 2021;522:167552. <https://doi.org/10.1016/j.jmmm.2020.167552>
10. Winger J, Schümann M, Kupka A, Odenbach S. Influence of the particle size on the magnetorheological effect of magnetorheological elastomers. *J Magn Magn Mater* 2019;481:176–82. <https://doi.org/10.1016/j.jmmm.2019.03.027>
11. Kaleta J, Królewicz M, Lewandowski D. Magneto-mechanical properties of anisotropic and isotropic magnetorheological composites with thermoplastic elastomer matrices. *Smart Mater Struct* 2011;20:085006. <https://doi.org/10.1088/0964-1726/20/8/085006>
12. Schubert G, Harrison P. Magnetic induction measurements and identification of the permeability of Magneto-Rheological Elastomers using finite element simulations. *J Magn Magn Mater* 2016;404:205–14. <https://doi.org/10.1016/j.jmmm.2015.12.003>
13. Vatandoost H, Sedaghati R, Rakheja S. A novel methodology for accurate estimation of magnetic permeability of magnetorheological elastomers. *J Magn Magn Mater* 2022;560:169669. <https://doi.org/10.1016/j.jmmm.2022.169669>
14. Lian C, Lee K, An J, Lee C. Effect of stick-slip on magneto-rheological elastomer with a magnetic field. *Friction* 2017;5:383–91. <https://doi.org/10.1007/s40544-017-0150-1>
15. Johari MAF, Mazlan SA, Nasef MM, Ubaidillah U, Nordin NA, Aziz SAA, et al. Microstructural behavior of magnetorheological elastomer undergoing durability evaluation by stress relaxation. *Sci Rep* 2021;11:10936. <https://doi.org/10.1038/s41598-021-90484-0>
16. Li Y, Li J, Li W, Du H. A state-of-the-art review on magnetorheological elastomer devices. *Smart Mater Struct* 2014;23:123001. <https://doi.org/10.1088/0964-1726/23/12/123001>
17. Bastola AK, Hossain M. A review on magneto-mechanical characterizations of magnetorheological elastomers. *Compos Part B Eng* 2020;200:108348. <https://doi.org/10.1016/j.compositesb.2020.108348>
18. Nguyen XB, Komatsuzaki T, Truong HT. Adaptive parameter identification of Bouc-wen hysteresis model for a vibration system using magnetorheological elastomer. *Int J Mech Sci* 2022;213:106848. <https://doi.org/10.1016/j.ijmecsci.2021.106848>
19. Wang P, Yang S, Liu Y, Zhao Y. Experimental Study and Fractional Derivative Model Prediction for Dynamic Viscoelasticity of Magnetorheological Elastomers. *J Vib Eng Technol* 2022;10:1865–81. <https://doi.org/10.1007/s42417-022-00488-x>
20. Nguyen XB, Komatsuzaki T, Zhang N. A nonlinear magnetorheological elastomer model based on fractional viscoelasticity, magnetic dipole interactions, and adaptive smooth Coulomb friction. *Mech Syst Signal Process* 2020;141:106438. <https://doi.org/10.1016/j.ymsp.2019.106438>
21. Nedjar A, Aguib S, Djedid T, Nour A, Settlet A, Tourab M. Analysis of the Dynamic Behavior of Magnetorheological Elastomer Composite: Elaboration and Identification of Rheological Properties. *Silicon* 2019;11:1287–93. <https://doi.org/10.1007/s12633-018-9921-1>
22. Wang B, Bustamante R, Kari L, Pang H, Gong X. Modelling the influence of magnetic fields to the viscoelastic behaviour of soft magnetorheological elastomers under finite strains. *Int J Plast* 2023;164:103578. <https://doi.org/10.1016/j.ijplas.2023.103578>
23. Metsch P, Kalina KA, Spieler C, Kästner M. A numerical study on magnetostrictive phenomena in magnetorheological elastomers. *Comput Mater Sci* 2016;124:364–74. <https://doi.org/10.1016/j.commatsci.2016.08.012>
24. Kukla M, Górecki J, Malujda I, Talaśka K, Tarkowski P. The Determination of Mechanical Properties of Magnetorheological Elastomers (MREs). *Procedia Eng* 2017;177:324–30. <https://doi.org/10.1016/j.proeng.2017.02.233>
25. Janbaz M, Saeidi Googarchin H. Experimental and numerical analysis on magneto-hyper-viscoelastic constitutive responses of magnetorheological elastomers: A characterization procedure. *Mech Mater* 2021;154:103712. <https://doi.org/10.1016/j.mechmat.2020.103712>
26. Asadi Khanouki M, Sedaghati R, Hemmatian M. Adaptive dynamic moduli of magnetorheological elastomers: From experimental identification to microstructure-based modeling. *Mater Sci Eng B Solid-State Mater Adv Technol* 2021;267. <https://doi.org/10.1016/j.mseb.2021.115083>
27. Yu Y, Li J, Li Y, Li S, Li H, Wang W. Comparative Investigation of Phenomenological Modeling for Hysteresis Responses of Magnetorheological Elastomer Devices. *Int J Mol Sci* 2019;20:3216. <https://doi.org/10.3390/ijms20133216>
28. Yu Y, Hoshyar AN, Li H, Zhang G, Wang W. Nonlinear characterization of magnetorheological elastomer-based smart device for structural seismic mitigation. *Int J Smart Nano Mater* 2021;12:390–428. <https://doi.org/10.1080/19475411.2021.1981477>
29. Li W, Zhou Y, Tian T, Alici G. Creep and recovery behaviors of magnetorheological elastomers. *Front Mech Eng China* 2010;5:341–6. <https://doi.org/10.1007/s11465-010-0096-8>
30. Versa 3D scanning electron microscope, Technical documentation 2023. <https://www.microscop.ru/uploads/VERSA3D.pdf> (accessed April 17, 2023)
31. Magnetometer LakeShore 7400 series, Technical documentation 2023. <https://www.lakeshore.com/products/categories/overview/discontinued-products/discontinued-products/7400-series-vsm> (accessed April 17, 2023)
32. FEMM 4.2, Technical documentation. 2023. <https://www.femm.info/wiki/Documentation/> (accessed April 17, 2023)
33. Gaussmeter GM2, Technical documentation 2023. <https://www.alphalabinc.com/product/gm2/> (accessed April 17, 2023).
34. Linear actuator, LA30-43-000A, Technical documentation 2023. <https://www.sensata.com/sites/default/files/a/sensata-voice-coil-actuator-linear-frameless-la30-43-000a-drawing.pdf> (accessed April 17, 2023)
35. 9063 CompactRIO Controller, Technical documentation 2023. <https://www.ni.com/pl-pl/support/model.crio-9063.html> (accessed April 17, 2023).
36. Linear encoder with sinus/cosinus output, LIKA SMS12, Technical documentation 2023. [http://www.lika.pl/pliki\\_do\\_pobrania/CAT%20SMS12%20E.pdf](http://www.lika.pl/pliki_do_pobrania/CAT%20SMS12%20E.pdf) (accessed April 17, 2023)
37. Snamina J, Orkisz P. Active vibration reduction system with mass damper tuned using the sliding mode control algorithm. *J Low Freq Noise Vib Act Control* 2021;40:540–54. <https://doi.org/10.1177/1461348420904257>
38. Wang DH, Liao WH. Magnetorheological fluid dampers: a review of parametric modelling. *Smart Mater Struct* 2011;20:023001. <https://doi.org/10.1088/0964-1726/20/2/023001>

This research was funded by the AGH University of Krakow within the scope of the research program No. 16.16.130.942.

Denys Gutenko:  <https://orcid.org/0000-0003-4160-724X>

Pawel Orkisz:  <https://orcid.org/0000-0002-8928-8455>

Bogdan Sapiński:  <https://orcid.org/0000-0001-6952-8303>

 This work is licensed under the Creative Commons BY-NC-ND 4.0 license.